3D-characterization of deuterium distributions in zirconium oxide scale using high-resolution SIMS

Kexue Li[1*], Thomas Aarholt[2], Junliang Liu[1], Helen Hulme[3], Alistair Garner[3], Michael Preuss[3], Sergio Lozano-Perez[1] and Chris Grovenor[1]

[1] Department of Materials, University of Oxford, Oxford, OX1 3PH, UK;
[2] Department of Physics, University of Oslo, Oslo, 0316, Norway;
[3] School of Materials, University of Manchester, Manchester, M13 9PL, UK
* Correspondence: kexue.li@materials.ox.ac.uk; Tel.: +44 (0)1865 2 73766

Academic Editor: name
Received: date; Accepted: date; Published: date

Abstract: In pressurised water reactors (PWRs), fuel rods are clad with zirconium alloy tubes chosen for their low neutron capture cross section and good oxidation resistance. Understanding cladding-water corrosion reactions at 280-350 °C and the correlated hydrogen pickup into these Zr alloys is crucial to the safe operation of PWRs and to increasing the burnup of the fuel. Here we describe a method based on 3D mapping by high resolution SIMS to measure the distribution of deuterium in oxidised Zircaloy-4 alloy samples. Two analysis directions, depth-profiling and cross-sectional, were used to ensure we understand possible imaging artefacts during sputtering of the complex microstructure in these samples. The topography of the sputtering carter and sputtering rate have been calibrated by Focused Ion Beam (FIB)/Scanning Electron Microscopy (SEM) analysis. The deuterium diffusion coefficients at 360 °C is calculated suing the depth profile in both samples. The results show that the 3D deuterium distribution can be successfully measured in isotopically spiked samples, but that care has to be taken to understand the effect of deuterium outgassing and surface diffusion during Cs^+ primary ion bombardment, which results in a degraded lateral resolution, which distorts the apparent deuterium distribution. The detection method in this paper can be a useful tool in the analysis of the distribution of hydrogenic species in zirconium fuel cladding materials in service, and can also provide other engineering materials.

Keywords: NanoSIMS, Deuterium, 3D-characterization, Zirconium oxidation, hydrogen uptake

1. Introduction

For many years zirconium alloys have been used as fuel cladding in the nuclear industry due to their low neutron capture cross section [1], reasonable mechanical properties and corrosion resistance [2]. However, hydrogen pickup (HPU) during corrosion of Zr alloys in contact with high-temperature water is still a major limiting factor for achieving high fuel burnup. Water dissociation by the cathodic reaction and radiolysis results in the creation of hydrogen atoms, some of which recombine to form H_2 that is released to the environment but the rest can penetrate into the Zr matrix, contributing to HPU [3]. If the hydrogen concentration exceeds the bulk solubility, brittle hydrides are formed in alloy matrix resulting in a reduction the cladding strength [4]. The pathways and mechanisms by which the hydrogen migrates through the oxide layer formed by aqueous corrosion on the Zr surface are still not well understood.

The inner, protective part of the oxide is reported to have a high electrical resistance, be impermeable by the electrolyte and to contain almost no hydrogen [5, 6]. Based on previous SIMS analysis of hydrogen distributions [7], compressive stress in this barrier layer has been suggested to suppress hydrogen diffusion in this region [8]. There have been several suggestions for the key mechanisms of hydrogen penetration through the barrier oxide. Second Phase Particles (SPPs) could provide a diffusion pathway [9-11], although they are usually too well separated to offer a continuous permeation path. Cracks and pores [12], interconnected porosity [13, 14] and oxide grain boundaries [15, 16] have all been described as preferential paths for both hydrogenic and oxidising species to reach the reacting metal surface. However, there is a lack of direct experimental data, especially on the 3D hydrogen distribution in the oxide, to support these mechanisms, partly because of the experimental difficulty of mapping hydrogen isotopes with high spatial resolution.

Finding an appropriate analytical technique is the key to solving this problem. Atom probe tomography (APT) allows the analysis of trace element distributions with a higher sensitivity than can be achieved by Transmission Electron Microscopy (TEM) analysis [17, 18], but this technique is limited by complicated sample preparation, and the relatively low mass resolution [19, 20] can also make it difficult to resolve interferences between different hydrogen-containing ionic species. Secondary Ion Mass Spectrometry (SIMS) depth profile analysis is very widely used to characterise elemental distributions in a variety of inorganic and organic samples [21-24] and has a high sensitivity for light elements. Combined focused ion beam secondary ion mass spectrometry (FIB-SIMS) [25, 26], and correlated secondary ion mass spectrometry and atomic force microscopy (SIMS-AFM) [27, 28] experiments have reported results on 3D elemental distributions, including of light elements. However, FIB-SIMS instruments sacrifice the performance of dedicated SIMS analysis, typically showing low ionisation and transmission efficiencies and relatively poor mass resolution. SIMS-AFM instruments can also have problems with measuring deep craters that result in tip damage. No 3D hydrogen/deuterium measurements have yet been reported, and there has been little discussion of possible distortion of the apparent distribution of trapped hydrogen as a result of bombardment by the intense primary beam.

We have recently shown that high-resolution SIMS analysis of oxidised zirconium alloys using a CAMECA NanoSIMS 50 instrument enables the mapping of hydrogen distributions on a sub-micrometre scale with minimal sample preparation [6]. However, the interpretation of hydrogen distributions in NanoSIMS analysis is challenging because the signal at one Dalton can originate from various external sources, including the vacuum system and surface contamination. In this study deuterium spiking as a surrogate for hydrogen is used as previously described [6], and our aim here is to present an analytical methodology that gives reliable data on the key mechanisms of hydrogen penetration through the thin oxide layer formed on zirconium alloy surfaces in service.

2. Materials and Methods

2.1. Sample Description

Two Zircaloy-4 alloy samples were used in this study. These were recrystallised sheet materials, initially supplied by Westinghouse Electric Company after oxidation in an autoclave at 360 °C and 18 MPa in pure water for 30 and 75 days. These samples were subsequently oxidised in pure heavy water for another 31 days in a similar autoclave at the University of Manchester. Z4-5, with a total oxidation time of 61 days was chosen to represent the pre-transition stage of oxidation before the first characteristic acceleration in corrosion rate caused by breakdown in the protective nature of the oxide. Z4-9 with a total oxidation time of 106 days was around the transition point in oxidation kinetics. The overall oxide thicknesses of the two samples were measured by FIB/SEM to be 1.9 μm and 2.2 μm for samples Z4-5 and Z4-9 respectively. Samples for depth-profiling were made simply by cutting the oxidised sheet material to

7 × 7 mm² using a slow speed diamond saw and loading into the NanoSIMS without any further pre-treatment. Cross-sectional samples were prepared by the method described in detail in ref [6]. Briefly, sheet samples were cut into 6x3 mm sections that were then glued together (oxide to oxide) in a single block to expose the cross-section of the metal oxide interface for both samples on one polished face. The block was cut to fit the NanoSIMS holder, and samples were ground flat using silicon carbide paper down to 4000 grit and subsequently polished over several hours using only water-diluted colloidal silica. A further colloidal silica polish was performed immediately before loading samples into the NanoSIMS to remove the native oxide that forms on the polished metal surface. Both depth-profiling and cross-sectional samples were coated with 5 nm of platinum to minimise charging from the insulating oxide layer and surrounding resin, and to provide a conducting pathway from the sample to the holder. **Figure 1** shows a schematic of the depth-profiling (panels a, c and e) and cross-sectional (panels b, d and f) analysis geometries arranged in the order of sample preparation, NanoSIMS analysis and FIB/SEM measurements. The direction of oxide growth is defined by the z-axes; the oxide surface and oxide/metal interface are parallel to the x-y plane, and the NanoSIMS measurement surfaces are the x-y plane and the y-z plane for depth-profiling and cross-sectional analysis, respectively.

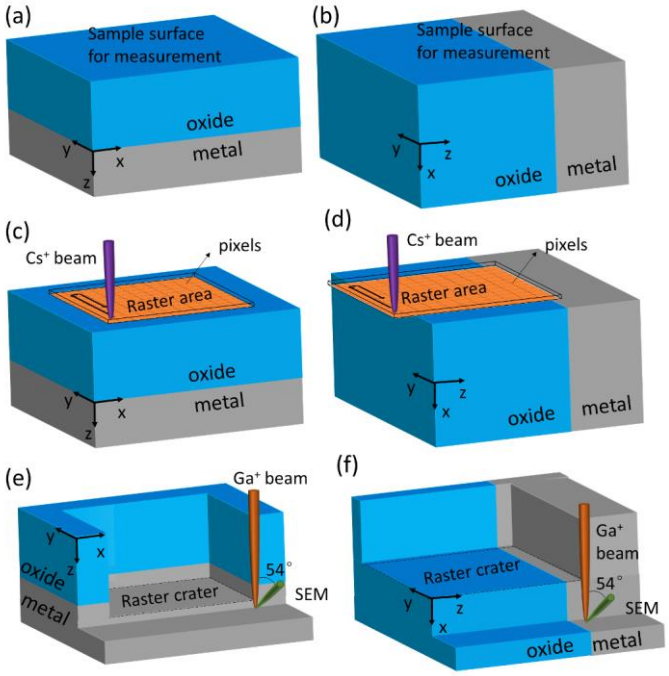

Figure 1. Schematic of sample preparation geometries for NanoSIMS analysis and FIB/SEM measurements. (a) and (b) are the depth-profiling and cross-sectional sample orientations, respectively, (c) and (d) the geometry of NanoSIMS measurements for depth-profiling and cross-sectional experiments, and (e) and (f) the geometry of FIB/SEM measurements for depth-profiling and cross-sectional experiments.

2.2. NanoSIMS analysis

High-resolution SIMS analysis was undertaken using a CAMECA NanoSIMS 50 with a 16 keV Cs^+ primary beam, and simultaneous secondary ion collection of $^2D^-$ and $^{16}O^-$ or $^{18}O^-$. It was often necessary to use the $^{18}O^-$ signal to protect the electron multipliers because from the oxide layer the $^{16}O^-$ ion yield can exceed 5×10^6 counts per second. **Figure 2** is a typical detail of a mass spectrum from a sample without the final deuteration treatment, and illustrates the clear separation of $^2D^-$ and H_2^- signals around 2 Daltons using a mass resolving power of about 1300, showing that unwanted contributions to a $^2D^-$ signal from H_2^- can be ignored under our typical analysis conditions. The lateral resolution of the secondary ion image is

controlled by the primary beam spot size, and a 3D dataset is built up by the collection of a large number of 2D images. This kind of 3D mapping is time-consuming, and depending on what precise experiment we are undertaking. **Figure 1** panel (c) and (d) show schematics of the geometry of the NanoSIMS measurements for depth-profiling and cross-sectional experiments respectively.

In order to reduce the overall experimental time while minimizing the amount of data collected, we have used what we term coarse-scan tuning with a small raster area (5×5 μm^2) and high primary beam dwell time per pixel analyzed (> 1000 μs/pixel). For samples Z4-5 and Z4-9, this reduces the measurement time through to the oxide/metal interface to less than 18 hours. The fine-scan tuning is used to obtain higher resolution data on the precise 3D deuterium distribution, so we used a larger raster area (10 × 10 μm^2) and shorter dwell time (300-1000 μs/pixel), which needs longer measurement times and generates a larger amount of data. The three different analytical settings are defined in Table 1. A large beam size to pixel size ratio (6-10) was used in all cases to ensure that the crater bottom is as flat as possible to help with accurate 3D data reconstruction.

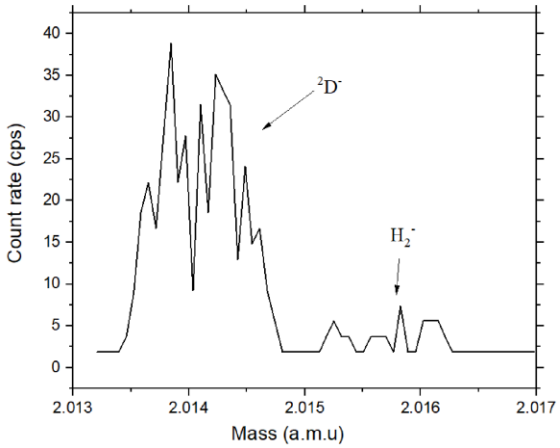

Figure 2. High-resolution mass spectra around two Daltons showing the $^2D^-$ and H_2^- peaks. The isotope ratio of D/H measured from this unspiked sample is 1.5×10^{-4}, close to the natural value. The units on the x-axis and y-axis are atomic mass units (a.m.u) and counts per second (cps), respectively.

Table 1. NanoSIMS settings for coarse and fine scans for depth-profiling, and for the cross-sectional scanning mode.

Scan mode	Coarse-scan	Fine-scan	Cross-sectional samples
Entrance slit	open	open	open
Aperture slit	open	open	open
D1 aperture (μm)	D1-2, 300	D1-2, 300	D1-3, 150
Lateral resolution (nm)	150-200	150-200	100-150
Raster size (μm^2)	25 (5×5)	100 (10×10)	64 (8×8)
Pixels	256×256	512×512	512×512
Beam size / pixel size	8-10	8-10	6-10
Dwell time (μs)	1000-5000	300	1000
Analysis time (h)	<18	50-70	50-70

2.3. FIB/SEM measurements

FIB sectioning of SIMS craters was carried out on a Zeiss Auriga 40 FIB/SEM instrument using 30 kV Ga^+ incident beam energy. **Figure 1** panel (e) and (f) show schematics of the geometry of the FIB/SEM measurements for depth-profiling and cross-sectional experiments respectively. Samples were orientated so that the focused Ga^+ ion beam was at normal incidence to the metal-oxide interface (depth-profiling measurement) and parallel to the metal-oxide interface (cross-sectional measurement). Before sectioning, a protective coating of platinum was deposited on the area of interest and then a staircase trench was made in front of the volume of interest. The front trench was made to reveal the cross-section to be imaged and to provide space to accommodate re-deposited materials during the sectioning process. A beam current of 1 nA was used to carry out the sectioning. SEM images of the crater depth and shape were taken at a tilt angle of 54°.

2.4. NanoSIMS data processing

To minimise edge-related effects during NanoSIMS analysis, we only chose the pixels more than 0.4 μm and 0.8 μm away from the edge of the image during coarse (5 × 5 μm^2 raster area) and fine analysis (10 × 10 μm^2 raster area), respectively. ImageJ with the OpenMIMS plugin (Harvard) [29] was used to read raw NanoSIMS data and create deuterium depth profiles and cross-sectional views. Mercury Avizo 9.2 is a software package that enables users to perform interactive visualization and computation on 3D data sets with an interface modelled on visual programming [30], and was used for 3D data reconstruction.

Depth profile plots of deuterium (see **Figure 5**) are created from 'Image' then 'Stacks' and 'Plot Z-axis Profile' routines. The x-axis is the number of images, and the y-axis is counts per pixel. Then the x-axis is converted from number of images to distance using the FIB/SEM measurements on the crater depth. Cross-sectional images (see **Figure 6**) are created from 'Image' then 'Stacks' and 'Reslice' routines, and then the x-axis is converted from number of images to distance using the FIB/SEM measurement.

3D data reconstruction:

1) Extracted stack data in ImageJ of deuterium, oxygen and secondary electron (SE) signals are saved as '*.raw' format files, separately, and then loaded into Avizo 9.2 for 3D reconstructions.
2) Oxygen and secondary electron (SE) signals are smoothed by the following steps: 'Image Processing' then 'Smoothing and Denoising' and 'Median Filter'. Then data is smoothed by averaging over 3 pixels to obtain a clear 3D oxide/metal interface.
3) Deuterium pixels are masked by the function 'Edit New Label Field'. Because the coarse measurements usually have high $^2D^-$ secondary ion signals, the pixels were separated into two groups; *high-count pixels* containing ≥ 4 $^2D^-$ counts, and *low-count pixels* containing fewer than four $^2D^-$ counts (see **Figure 8**). For fine-scan measurement data, the $^2D^-$ ion signals are low and the pixels which contain ≥ 2 counts are used to do the 3D reconstruction (see **Figure 9**).
4) The masking pixels are generated and showed as a 3D surface by functions 'Generate surface' and 'Show surface', sequentially.

3. Results and discussion

3.1. The topography of crater bottom

To obtain an accurate 3D-characterization of deuterium from a stack of 2D images (planes) it is necessary to consider the topography of the crater bottom and the different sputter rates of the phases or crystallographic orientations encountered during sputtering **[31, 32]**. Since the zirconium dioxide grain size (30-40 nm in diameter [33]) is much smaller than the incident Cs^+ primary beam diameter (200 nm with aperture D1-2), we supposed that crystallographic effects in the oxide layer were unlikely to have a strong influence on the sputtering process. To confirm this, we carried out three tests in the depth-profiling geometry, with 2 × 2 μm^2, 5 × 5 μm^2 and 10 × 10 μm^2 raster areas to measure the topography of the resulting

crater. The results are shown in **Figure 3**, and the solid yellow lines mark the position of the metal/oxide interface in each case. Image (a) is for raster area 2 × 2 μm² and the bottom surface of the crater is located in the middle of the oxide. Image (b) is for raster area 5 × 5 μm² and the bottom surface is closer to the top of the oxide. Images (c) and (d) for raster area 10 × 10 μm² used a longer analysis time, and the crater bottom is near the oxide/metal interface. While in the oxide the bottom of the crater remains flat during sputtering, but as soon as the primary ion beam reaches the oxide/metal interface and the underlying Zr alloy is exposed, the higher sputtering rate of the metal rapidly creates a hole, and as shown in **Figure 3** (d) a complex topography is created at the bottom of the crater.

For cross-sectional samples, typical topography craters are shown in **Figure 3** (e) and (f). It is clear that the top edge of the oxide (left hand side of the images) has been sputtered away much faster than the bulk oxide, the well-known edge effect in sputter analysis [34], and that the metal also shows uneven sputtering since grains with different crystallographic orientation show different sputter yields.

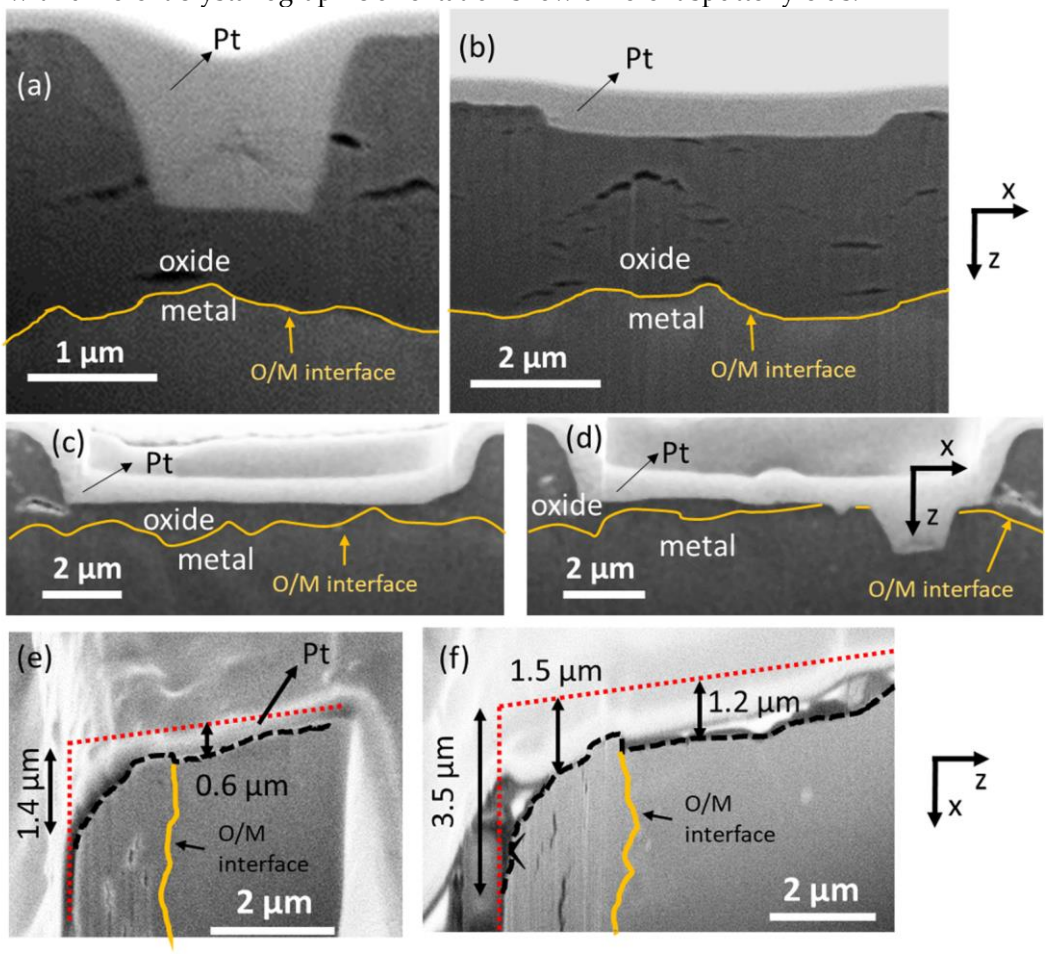

Figure 3. Cross section FIB/SEM views of NanoSIMS raster craters. Depth profiling samples at different locations are shown for raster areas (a) 2 × 2 μm², (b) 5 × 5 μm² and (c and d) 10 × 10 μm². Images (e) and (f) are the raster craters in cross-sectional samples of Z4-5 and Z4-9, respectively. Solid yellow lines mark the position of the oxide/metal interface. The dashed black lines show the bottom of the crater in (e) and (f), and the dotted red lines show the original sample surface before SIMS analysis.

In order to compare the topography of the crater bottom to the raster size, the surface roughness of the crater bottom was calculated from the arithmetic mean of the absolute ordinate values Z(x) within a sampling length (ISO 4287-1997) using Equation 1:

$$R_a = \frac{1}{l_w}\int_0^{l_w}|Z(x)|dx \quad (1)$$

where $Z(x) = \overline{Z_0} - Z_0(x)$, l_w is the length of crater bottom in a cross-section image and Z_0 is the measured ordinate along the z-axis. The results show that in the oxide, after high overlap beam sputtering, the crater bottom is very smooth. The crater bottom roughness is measured to be 9 ± 5, 15 ± 8 and 64 ± 25 nm for raster sizes 2 × 2, 5 × 5 and 10 × 10 μm, respectively. Compared to the large sputtering volumes in this work, and our focus on 3D reconstruction of the deuterium distribution in the oxide phase, this small roughness can be ignored, and we have applied no topographic corrections in this paper.

3.2. Sputtering rate

We have previously shown in 3D analysis of oxidised Zr alloys that cracks and porosity can be distributed in different locations from the sample surface to the oxide/metal interface [35]. Thus, in order to establish an accurate depth ordinate it is important to have a precise measure of the sputtering rate at different depths, defined as the time required to sputter a measured depth of the ZrO_2 matrix using known primary ion beam current for a given raster area (ISO 18115-1:2013(E)):

$$\text{Sputtering rate} = \frac{sputtered\ depth \times raster\ area}{primary\ beam\ current \times sputter\ time}\ (\frac{\text{nm} \times \mu m^2}{pA \times s}) \quad (2)$$

Table 2 shows a series of analyses using various sputtering times (150 to 1000 planes) but with all other parameters, dwell time (1000 μs), raster area (5 × 5 μm²), 256 × 256 pixels, remaining constant. The sputter rates at each different sputter depth were then calculated from Equation 3:

$$\mathrm{R}_i = \frac{D_i \times S}{FCo_i \times pix \times dt \times n_i} \quad (3)$$

where R_i is the average sputter rate and i is the analysis number, D_i is the sputtering depth, S is the raster area, n_i is the number of planes in analysis i, FCo_i is the primary beam current on the sample, pix is the number of pixels in each plane and dt is the dwell time on each pixel. FCo_i was determined from the primary column current FCp from equation 4:

$$FCo_i = \frac{FCp_i \times FCo_0}{FCp_0} \quad (4)$$

where FCo_0 and FCp_0 are the measured sample primary current and column current before the start of the measurement. FCp_i was monitored in each analysis from equation 5:

$$FCp_i = \frac{FCp_{i\_begin} + FCp_{i\_end}}{2} \quad (5)$$

where FCp_{i_begin} and FCp_{i_end} are the measured column current before and after each analysis.

The sputtering rates in Table 2 are the same within experimental error for different sputtering depth and samples after different corrosion time (and so different oxide thicknesses), showing that in this study that the distribution of cracks and porosity has little influence on the sputtering rate. The average sputtering rates in the ZrO_2 matrix are 0.20 ± 0.03 and 0.19 ± 0.04 (nm×um²)/(pA×s) for samples Z4-5 and Z4-9, respectively. Errors in this calibration mainly result from the crater depth measurement by SEM/FIB, due to image drift in the insulating sample, and also from fluctuations in measured primary ion current due to the variation of Faraday cup (FCo) detection efficiency and Cs^+ ion source stability during long-term measurements (3 to 18 hours). Due to the measured constant sputtering rate in both samples and at various sputtering depths, we concluded that there was no need to include a sputtering rate calibration in the depth profile and 3D reconstructions in this study.

238 Table 2. Measurement parameters and the sputtering rates in each analysis of samples Z4-5 and Z4-9.

Analysis name	Number of planes	FCp before analysis (pA)	FCp after analysis (pA)	Average FCp (pA)	FCo (D1-2) (pA)	Average depth (μm)	Error (2σ)	Total Cs^+ (dose/μm^2)	Sputtering rate (nm×μm^2/pA/s)	Error (2σ)
Z4-5										
201808_12	150	15650	17070	16360	3.25*	0.27	0.07	7.98×10^9	0.21	0.06
201808_15	269	14290	14450	14370	2.85	0.37	0.10	1.26×10^{10}	0.18	0.05
201808_13	300	17060	16270	16665	3.31	0.52	0.08	1.63×10^{10}	0.20	0.03
201808_14	450	16270	14290	15280	3.04	0.82	0.05	2.24×10^{10}	0.23	0.01
201808_16	600	14450	15900	15175	3.01	1.08	0.03	2.96×10^{10}	0.23	0.01
201808_17	750	15860	14470	15165	3.01	1.13	0.03	3.70×10^{10}	0.19	0.01
201808_18	1000	14450	13240	13845	2.75	1.39	0.13	4.50×10^{10}	0.19	0.02
Average									0.20	0.03
Z4-9										
201808_6	150	19490	18790	19140	3.73*	0.33	0.06	9.16×10^9	0.23	0.04
201808_7	300	18800	17370	18085	3.52	0.59	0.06	1.73×10^{10}	0.21	0.02
201808_8	450	17370	17080	17225	3.36	0.69	0.05	2.47×10^{10}	0.18	0.01
201808_9	600	17070	16190	16630	3.24	0.99	0.16	3.18×10^{10}	0.19	0.03
201808_10	750	16180	16450	16315	3.18	1.17	0.12	3.90×10^{10}	0.19	0.02
201808_11	1000	16440	14410	15425	3.01	1.31	0.15	4.92×10^{10}	0.17	0.02
Average									0.19	0.04

239 * FCo_0 is the measured FCo current (primary current on sample) before measurement. Other values of FCo are calculated from
240 FCo_0 using Equation 4.

241 *3.3. 1D depth profiles and deuterium diffusion coefficient*

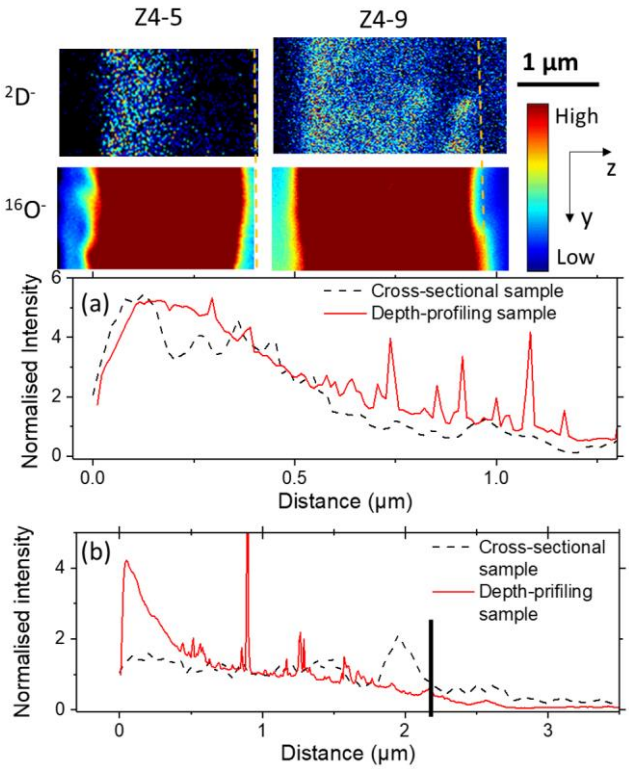

Figure 4. Secondary ion images ($^{2}D^{-}$ and $^{16}O^{-}$) taken from cross-sectional analysis, and the comparison of line profiles for the $^{2}D^{-}$ signal from cross-sectional and depth-profiling samples for (a) Z4-5 and (b) Z4-9. The secondary ion images are the sum of 5 images. The metal substrate is on the right-hand side of the upper ion images and the yellow dashed lines mark the approximate positions of the oxide/metal interface. The intensities of $^{2}D^{-}$ in the position 1 µm are normalised to 1. The black lines in (b) mark the position of the oxide metal interface.

Figure 4 top images show the secondary ion images ($^{2}D^{-}$ and $^{16}O^{-}$) from cross-sectional analysis of samples Z4-5 and Z4-9. To avoid topography effects, the results only show data collected before the oxide edge is sputtered away. In both samples, there is a gradual decrease in deuterium concentration from the outer part of the oxide towards the metal/oxide interface, with occasional abrupt increases in $^{2}D^{-}$ signal. The lower plots in **Figure 4** bottom plots compare directly the $^{2}D^{-}$ line profiles extracted from cross-sectional and depth-profiling samples for (a) Z4-5 and (b) Z4-9. Since the general form of the deuterium distribution is so similar from the cross-sectional and depth-profiling experiments, we can be confident that we have avoided major sputtering artefacts, apart from for Z4-9 the absence of the initial $^{2}D^{-}$ peak near the oxide surface which is a result of preferential sputtering of the top surface of the oxide away, in **Figure 3** image f. The $^{2}D^{-}$ peak just above the metal/oxide interface in the cross sectional analysis of Z4-9 appears much broader than the sharp peaks in the depth-profiling samples, but this is because resolution in the z direction in the depth-profiling samples is controlled by atomic mixing (~ 20 nm) during Cs^{+} ion bombardment and by the primary beam diameter in the cross sectional analysis (100-150 nm).

The diffusion behaviour of hydrogen/deuterium through the oxide layer contributes to determining the HPU performance of the cladding [36]. An estimate of the diffusion coefficient of deuterium in our samples was calculated by fitting the $^{2}D^{-}$ depth profile (red dotted line the NanoSIMS in-depth measurement in **Figure 5**) with the appropriate solution to Fick's 2nd law [37]:

$$\frac{C\,(X)}{C_s} = \left(1 - \frac{C_m}{C_s}\right) \cdot erfc\left(\frac{X}{2\sqrt{D_a t}}\right) + \frac{C_m}{C_s} \qquad (6)$$

with C(X) as the deuterium concentration at a distance X from the water/oxide interface, C_s the deuterium concentration at the water/oxide interface, C_m the concentration of deuterium pre-existing in the metal, erfc the complementary error function, D_a the deuterium diffusion coefficient and t the time the sample has been oxidised in heavy water (D_2O) which is 31 days in this study for both samples. All the deuterium concentrations are normalised by the concentration at the outer surface, C_s. Fitting to this equation yields diffusion coefficients of about 10^{-20} m²/s at 360 °C, very close to previous experimental results that lie between 10^{-18} and 10^{-21} m²/s [38-41]. Our results show that the pre-transition sample Z4-5 (61 days corrosion time) has a higher deuterium diffusion coefficient of $9.1 \pm 0.2 \times 10^{-20}$ m²/s than that in sample Z4-9 (106 days corrosion time) of $5.4 \pm 0.2 \times 10^{-20}$ m²/s. This is agreement with previous reports that the instantaneous hydrogen pickup fraction decreases just before the transition in oxidation rate [42].

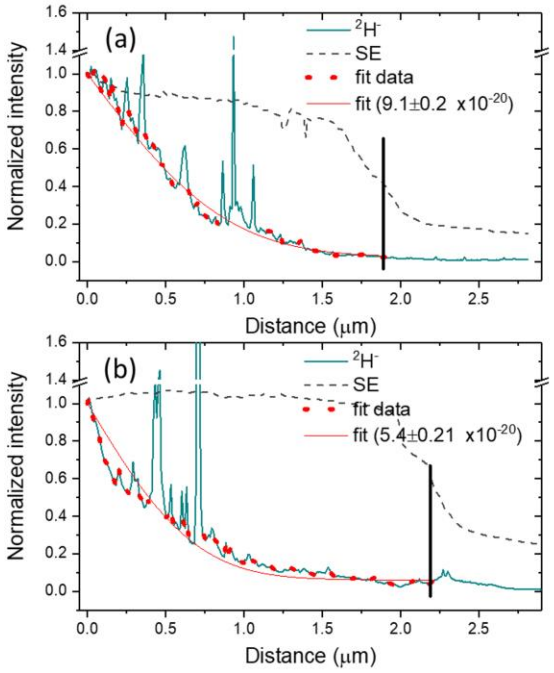

Figure 5. Initial fitting calculations of the diffusion coefficient of deuterium through the oxide using Fick's 2nd law on depth profile results from sample Z4-5 (a) and Z4-9 (b). The intensities of $^2D^-$ and secondary electron are normalised by the intensity at the surface (0 μm). The vertical black lines mark the position of the oxide metal interface.

3.4. 2D view images and the shape of hot deuterium spots

There is no suitable ZrO_2 standard to measure the depth resolution for $^2D^-$ secondary ions. Here the depth resolution is influenced by atomic mixing effects during the sputtering process resulting from the interaction of the energetic Cs^+ ions with the sample surface [34]. SRIM [43] simulations for 16 keV Cs^+ ion implantation suggest an ion range around 20 nm in zirconium dioxide. Considering the non-uniform sputtering effects within the analysed area due to inhomogeneous primary ion current density [34] is very low, the total depth resolution might be expected to be 20 nm.

From the 1D depth profiles in **Figure 5**, we can see there are many sharp peaks above the deuterium background. In the 2D image perpendicular to the Cs^+ beam direction in **Figure 6**, it is clear that these peaks are from apparent deuterium hot spots 1 to 2 μm in diameter and tens of nanometres in thickness. These types of hot deuterium spots are not only found in the in-depth analysis (a-d) both in coarse and fine scans, but also shown in the cross-sectional analysis in Figure 6 (e). However the shape of the hot spots is not the

same in the 2 analysis directions; both are lenticular, but with the long axes in the x-y plane in the in-depth analysis and in the x-z plane in the cross-sectional analysis. **Figure 7** shows a typical single deuterium hot spot in sample Z4-5. The thickness of each image/scan is simply calculated by dividing the oxide thickness by the total number of images, 3100 in this case. We define the location of the maximum $^2D^-$ intensity as 0 nm in depth, and the images above and below this point are treated as negative and positive locations. $^2D^-$ images from five different depths (-6 nm, -4 nm, 0 nm, 4 nm and 6 nm) are shown at the bottom of Figure 7. The upper plots are profiles in the $^2D^-$ signal in depth and laterally. The top right plot shows line scans across images at -4nm, 0 nm and 4 nm, with an apparent hot spot radius of 1-2 μm, and the line scan data are fitted by a Gaussian. In the top left plot, it is clear that the apparent thickness of the hot spot is around 15 nm, similar to the depth resolution estimated above. During the sputtering process, the deuterium hot spots appear and disappear quickly, and seem to have a lenticular shape that is microns in diameter but only tens of nanometres thick in the direction of Cs^+ beam analysis.

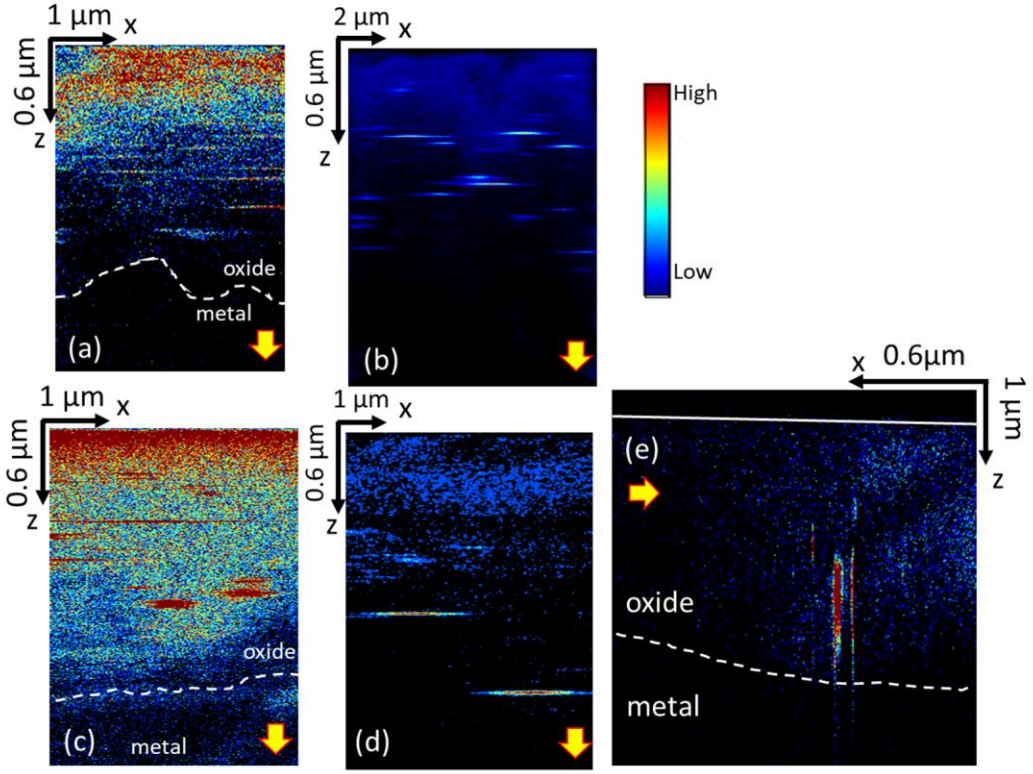

Figure 6. 2D $^2D^-$ ion images perpendicular to the Cs^+ beam direction. Image (a-d) are the results of in-depth analysis with the Cs^+ ion beam perpendicular to the water/oxide interface. Images (a) and (b) are coarse and fine scan results of sample Z4-5, respectively. Images (c) and (d) are coarse and fine scan results of sample Z4-9. Image (e) is a cross-sectional analysis of sample Z4-9 with the Cs^+ ion beam parallel to the water/oxide interface. White dashed lines mark the oxide/metal interface. Yellow arrows indicate the direction of incidence of the Cs^+ primary ion beam.

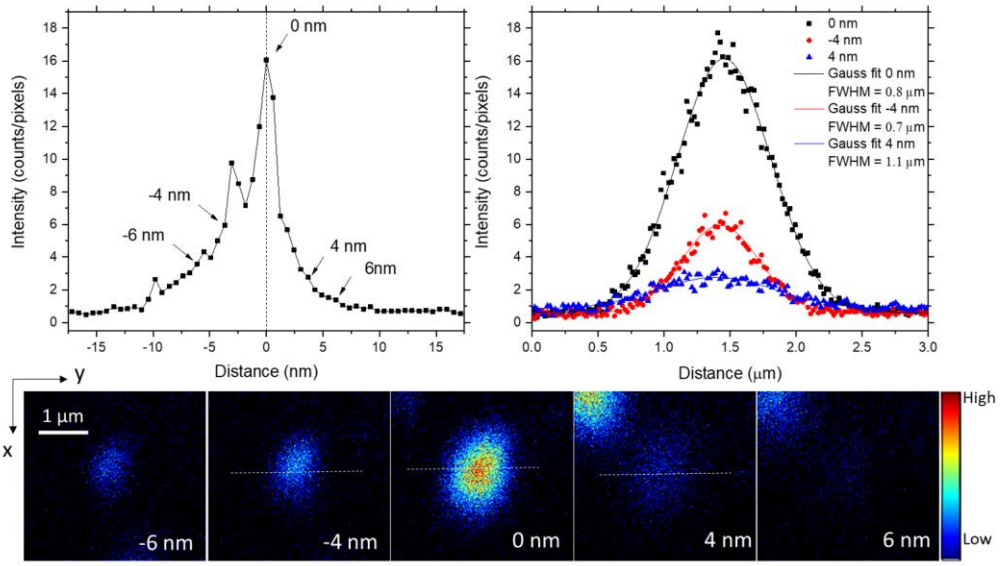

Figure 7. The bottom images are details of 2D deuterium ion images at 5 depths along the Cs^+ beam direction. The depth at the maximum $^2D^-$ intensity defined as 0 nm, and above and below this position are defined as negative and positive values of depth. The top left plot shows the depth profile through the deuterium hot spot in the centre of these images, and the top right plot shows line scans across the hot spot.

We have considered possible explanations for the apparent difference in shape of the deuterium hot spots in the two analysis directions, assuming that these must be the same microstructural features trapping deuterium in the oxide. One obvious explanation is the difference between lateral resolution (>150 nm) and depth resolution (~20 nm) in these experiments. If we compare the two hot spots rotated to the same orientation, the size of the overlapping volume is a few tens of nanometres in diameter. Another explanation is the suggested processes of hydrogen outgassing and diffusion during Cs^+ ion bombardment that creates an 'analysis zone' where the primary beam modifies the sample surface. In a NanoSIMS measurement, heat accumulates in the region bombarded by the highly focused primary ion beam. Ishitani and Kaga [44] and Schmied et al [45] predict that the local temperature increase could be as high as hundreds of degrees in a sample with poor thermal conductivity like zirconium dioxide. Using a range for 16 keV Cs^+ ions of 20 nm in zirconium dioxide, and taking the incident beam size to be ~150 - 200 nm, the volume of material that will transiently experience a significant increase in temperature is estimated to be 3.5×10^5 to 6.3×10^5 nm^3. Bringing these factors together, we suggest that when this analysis zone reaches a region of the microstructure in which deuterium is trapped, deuterium atoms will become mobile and diffuse to the surface resulting in a measured depth (15 nm) that is slightly less than the thickness of atom mixing layer (20 nm). Moreover, another evidence is the asymmetry of the peak with up and down. When the beam reaching deuterium reached area, the hot spot appears gradually and as more Cs^+ ion energy deposited in this area, the movement of deuterium is enhanced, then results in the disappearance of the hot spot faster. The area of the surface influenced by this outgassing and diffusion process is then convoluted with the incident Cs^+ beam size, resulting in the analysis of a deuterium-rich region with a horizontal diameter much larger than the scale of the original trapping site. Obviously, when we analyse the samples in the depth-profiling and cross-sectional directions, this process will result in the same deuterium-rich regions having lenticular shapes oriented differently with respect to the metal/oxide interface.

3.4. 3D deuterium reconstruction

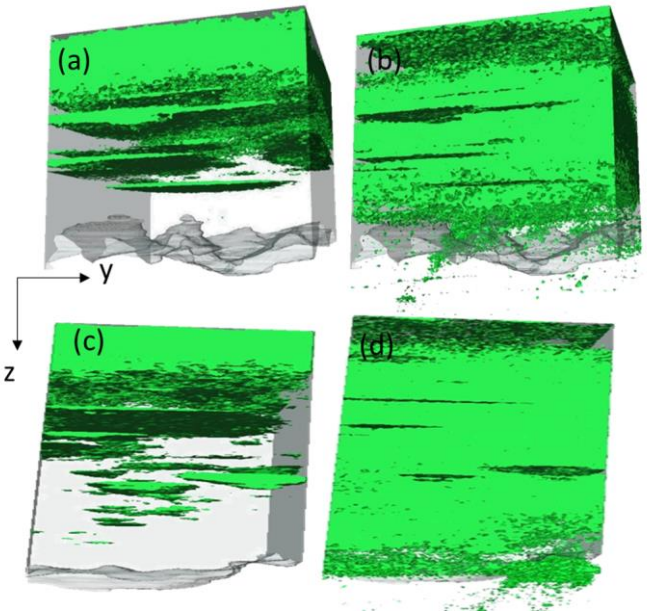

Figure 8. Typical 3D distributions of $^{2}D^{-}$ from the coarse scan analysis of samples Z4-5 (a and b) and Z4-9 (c and d). (a) and (c) are high-count pixel images, and (b) and (d) are low-count pixels images. The calibrated imaged volumes were x = 3.8 μm, y = 3.8 μm and 3D-z = 1.9 μm (oxide) for sample Z4-5, and x = 2.6 μm, y = 2.2 μm and z = 2.2 μm (oxide) for sample Z4-9.

For each sample, we have analysed in this study, we detect well-defined, broad peaks in the $^{2}D^{-}$ signals near the surfaces of the depth profiles (**Figure 4**) that correspond well with the volume at the top of the 3D images in **Figure 8** (a) and (c), where almost every pixel contains > 4 counts, indicating the region of the oxide with the highest levels of trapped deuterium. Overlaid on the gradual decrease in deuterium concentration with depth, there are sharp spikes in the $^{2}D^{-}$ signal in **Figure 5** that correspond to the apparently planar 'hotspots' in the cross section view **Figure 6**, and disk-shaped features in the 3D representation in **Figure 8** (a) and (c). $^{2}D^{-}$ ion signals are also found around the oxide/metal interface suggesting deuterium penetration into the metal substrate in the low-count image in **Figure 8** (d). References [37, 46] describe how at the oxide/metal interface hydrogen is reduced and accumulates into the metal and will precipitate as zirconium hydrides if the solubility limit is exceeded.

According to previous reports, the multiple phases at, and roughness of, the oxide/metal interface could result in different sputtering behaviours caused by the exposure of different material surfaces and topographies [31], and this might cause strong variations in $^{2}D^{-}$ ion yield during sputtering – the so-called matrix effect. However, when we compare low-count pixel image in **Figure 8** images (b) and (d) at the oxide/metal interfaces in our two samples at different oxidation stages, Z4-9 shows a thicker deuterium-rich layer than the earlier sample Z4-5 (where we can detect no $^{2}D^{-}$ signal at all), and it seems unlikely that this difference can be simply explained by the matrix effect.

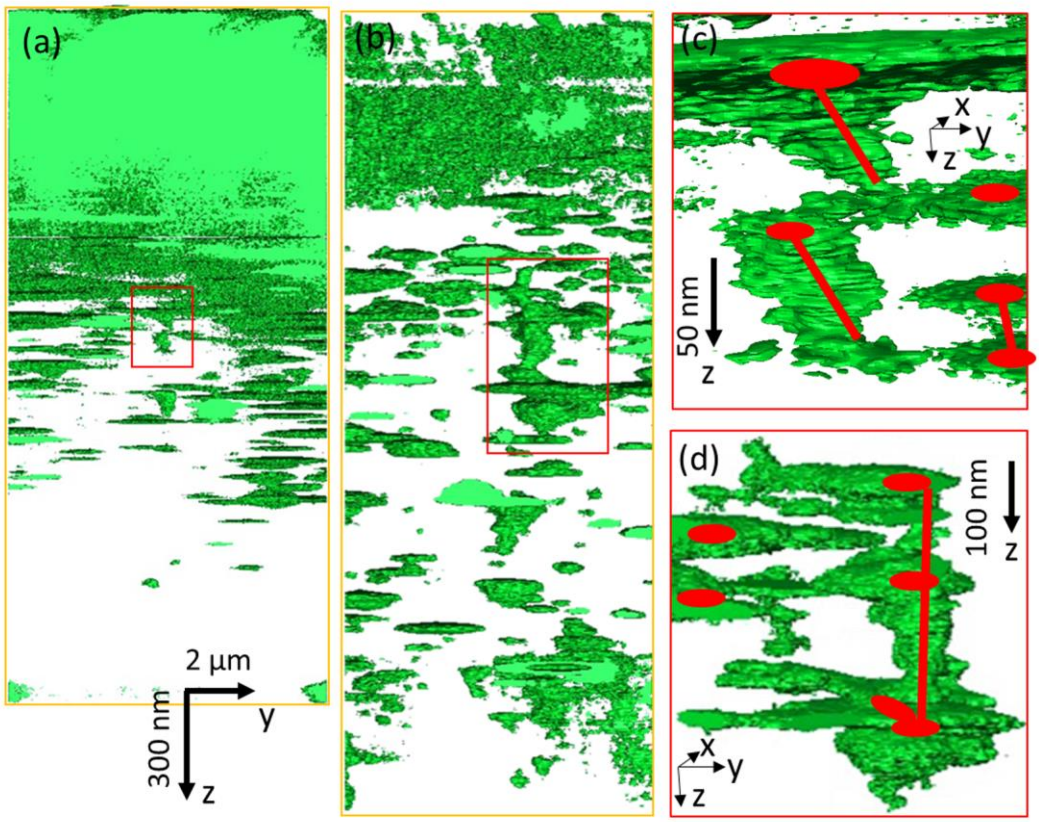

Figure 9. Typical 3D distributions of $^{2}D^{-}$ from fine scan analysis of samples Z4-5 (a) and Z4-9 (b) in the y-z view with the z direction stretched for clarity. (c) and (d) are magnified images of the red boxes in (a) and (b) respectively. The green volume represents the measured 3D distributions of deuterium, the red spots represent our suggested real deuterium distribution in the oxide and the red lines possible deuterium transport paths.

The coarse-scan measurements described above can give useful information on the deuterium distributions, but information can be lost in the 3D reconstructions due to the small raster area. Therefore we designed a fine-scan measurement protocol with larger raster area (10×10 µm²) and shorter dwell time (300 µs/pixel) that required much longer measurement times, usually 50 – 70 hours to penetrate down to the metal/oxide interface. Increasing the scan speed can reduce the deuterium degassing effect because the local temperature rise will be reduced. More details of the deuterium distribution can be seen in the 3D reconstructions for the fine-scan experiments in **Figure 9** than in the coarse-scan experiments in **Figure 8**. For instance, both magnified images, **Figure 9** (c) and (d), show over a distance of about 120 nm a suggestion of a vertical pathway connecting three $^{2}D^{-}$ hotspots. A similar possible pathway can be seen immediately below the red box in (c).

Due to the imaging artefacts discussed above, we have to be aware that these detailed 3D reconstructions of the deuterium distribution suggest larger trapping volumes than the real deuterium distribution in the oxide. In the magnified images in **Figure 9** (c) and (d), we suggest with red spots what size the real deuterium trapping volumes might be, and can also see that some of these hot spots may be connected by narrow pathways of high deuterium concentration, which could be regions of interconnected porosity in the oxide as previously observed in similar samples [13]. In future research, detailed modelling of hydrogen/deuterium movements during Cs^{+} beam sputtering will be needed to estimate the precise hydrogen/deuterium trapping volumes and diffusion pathways.

4. Conclusions

We have presented an analytical method using high-resolution secondary ion mass spectrometry to characterise with sub-micron resolution the 3D distribution of deuterium in Zircaloy-4 samples oxidised in high-temperature heavy water. The key findings are:

1. Careful calibration of the sputtering process has allowed us to measure the sputtering rates in different depth in both samples, and find that effects due to cracks and porosity can be ignored. The average sputtering rates in the ZrO_2 matrix are 0.19 ± 0.04 and 0.20 ± 0.03 $(nm \times um^2)/(pA \times s)$ for samples Z4-5 and Z4-9, respectively and the sputtering rate is constant at different depths in both samples. We also estimate the depth resolution of NanoSIMS measurements in the oxide to be no more than 20 nm, controlled by atomic mixing effects.
2. We have explored different analytical conditions for depth-profiling, coarse- and fine-scans, and have shown that because of the larger raster area and shorter dwell time, the fine-scan results can give higher resolution information on the deuterium distribution.
3. By comparing cross-sectional and depth profiling experiments on the same materials, and by measuring the imaging artefacts that result from a primary beam that is much larger than the intrinsic depth resolution, we have determined the true morphology of the strong deuterium trapping sites in the oxide.
4. With this detailed understanding of the experimental conditions, we have been able to show that the deuterium is highly concentrated in the fossil oxide near the water/oxide interface, and there is a gradual decrease in trapped deuterium in the denser oxide towards the oxide/metal interface with abrupt peaks in $^2D^-$ signal that are evidence for local trapping sites like small cracks and porosity [13, 14] linked by diffusion paths through which the deuterium can penetrate through to the metal matrix.
5. Confidence in this analysis is given by the fact that the deuterium diffusion coefficients at 360 °C calculated using the depth profile in both pre-transition ($9.1 \pm 0.2 \times 10^{-20}$ m^2/s) and near-transition samples ($5.4 \pm 0.2 \times 10^{-20}$ m^2/s) agree well with previous experimental results.

We propose that experiments of this kind can be used to generate a better understanding of the key mechanism that control HPU in zirconium fuel cladding materials in service, and can also provide a useful tool in the analysis of the distribution of hydrogenic species in other engineering materials.

Acknowledgements

The authors acknowledge the contribution made to this work by their collaborators from Westinghouse and the MUZIC-2 project providing zirconium samples. This study is funded by the UK Engineering and Physical Sciences Research Council under grant EP/M018237/1. Thomas Aarholt is grateful for support from Westinghouse. Helen Hulme is grateful for funding from AMEC-Foster Wheeler, Alistair Garner and Michael Preuss are grateful for funding from the UK Engineering and Physical Sciences Research Council under grants EP/L018616/1 and EP/I005420/1. The authors acknowledge James Marrow for access to facilities to create the 3D images.

References

[1] S. Nakamura, H. Harada, S. Raman, P.E. Koehler, Thermal neutron capture cross sections of zirconium-91 and zirconium-93 by prompt gamma-ray spectroscopy, J Nucl Sci Technol, 44 (2007) 21-28.

[2] S. Kass, The development of the zircaloys, in: Corrosion of Zirconium Alloys, ASTM International, 1964, pp. 3-27.

[3] B. Cox, A mechanism for the hydrogen uptake process in zirconium alloys, J Nucl Mater, 264 (1999) 283-294.

[4] D. Northwood, U. Kosasih, Hydrides and delayed hydrogen cracking in zirconium and its alloys, International Metals Reviews, 28 (1983) 92-121.

[5] A.J. Maroto, R. Bordoni, M. Villegas, A.M. Olmedo, M. Blesa, A. Iglesias, P. Koenig, Growth and characterization of oxide layers on zirconium alloys, J Nucl Mater, 229 (1996) 79-92.

[6] S.S. Yardley, K.L. Moore, N. Ni, J.F. Wei, S. Lyon, M. Preuss, S. Lozano-Perez, C.R.M. Grovenor, An investigation of the oxidation behaviour of zirconium alloys using isotopic tracers and high resolution SIMS, J Nucl Mater, 443 (2013) 436-443.

[7] M.B. Elmoselhi, B.D. Warr, S. McIntyre, A study of the hydrogen uptake mechanism in zirconium alloys, in: Zirconium in the Nuclear Industry: Tenth International Symposium, ASTM International, 1994, pp. 62-77.

[8] K. Une, K. Sakamoto, J. Matsunaga, Y. Etoh, M. Aomi, I. Takagi, K. Sawada, H. Watanabe, Controlling factors in hydrogen absorption of zirconium alloys, Proceedings of TopFuel, (2012) 2-6.

[9] P. Bossis, G. Lelievre, P. Barberis, X. Iltis, F. Lefebvre, Multi-scale characterization of the metal-oxide interface of zirconium alloys, in: Zirconium in the Nuclear Industry: Twelfth International Symposium, ASTM International, 2000, pp. 918-942.

[10] K. Baur, F. Garzarolli, H. Ruhmann, H. Sell, Electrochemical examinations in 350 C water with respect to the mechanism of corrosion-hydrogen pickup, in: Zirconium in the Nuclear Industry: Twelfth International Symposium, ASTM International, 2000, pp. 836-851.

[11] Y. Hatano, K. Isobe, R. Hitaka, M. Sugisaki, Role of intermetallic precipitates in hydrogen uptake of Zircaloy-2, J Nucl Sci Technol, 33 (1996) 944-949.

[12] B. Cox, Y.M. Wong, A hydrogen uptake micro-mechanism for Zr alloys, J Nucl Mater, 270 (1999) 134-146.

[13] N. Ni, S. Lozano-Perez, M.L. Jenkins, C. English, G.D.W. Smith, J.M. Sykes, C.R.M. Grovenor, Porosity in oxides on zirconium fuel cladding alloys, and its importance in controlling oxidation rates, Scripta Mater, 62 (2010) 564-567.

[14] N. Ramasubramanian, V. Perovic, M. Leger, Hydrogen Transport in the Oxide and Hydrogen Pickup by the Metal During Out-and In-Reactor Corrosion of Zr-2.5 Nb Pressure Tube Material, in: Zirconium in the Nuclear Industry: Twelfth International Symposium, ASTM International, 2000, pp. 853-876.

[15] G. Sundell, M. Thuvander, A. Yatim, H. Nordin, H.-O. Andrén, Direct observation of hydrogen and deuterium in oxide grain boundaries in corroded Zirconium alloys, Corros Sci, 90 (2015) 1-4.

[16] A. Garner, J. Hu, A. Harte, P. Frankel, C. Grovenor, S. Lozano-Perez, M. Preuss, The effect of Sn concentration on oxide texture and microstructure formation in zirconium alloys, Acta Mater, 99 (2015) 259-272.

[17] M.P. Moody, A. Vella, S.S.A. Gerstl, P.A.J. Bagot, Advances in atom probe tomography instrumentation: Implications for materials research, Mrs Bull, 41 (2016) 40-45.

[18] G. Sundell, M. Thuvander, H.O. Andren, Barrier oxide chemistry and hydrogen pick-up mechanisms in zirconium alloys, Corros Sci, 102 (2016) 490-502.

[19] R. Gemma, T. Al-Kassab, R. Kirchheim, A. Pundt, Analysis of deuterium in V-Fe5at.% film by atom probe tomography (APT), J Alloy Compd, 509 (2011) S872-S876.

[20] D. Haley, S.V. Merzlikin, P. Choi, D. Raabe, Atom probe tomography observation of hydrogen in high-Mn steel and silver charged via an electrolytic route, Int J Hydrogen Energ, 39 (2014) 12221-12229.
[21] J.N. Audinot, A. Hamdan, P. Grysan, Y. Fleming, C. Noel, F. Kosior, G. Henrion, T. Belmonte, Combined SIMS and AFM study of complex structures of streamers on metallic multilayers, Surf Interface Anal, 46 (2014) 397-400.
[22] S. Ghosal, S.J. Fallon, T.J. Leighton, K.E. Wheeler, M.J. Kristo, I.D. Nutcheon, P.K. Weber, Imaging and 3D elemental characterization of intact bacterial spores by high-resolution secondary ion mass spectrometry, Anal Chem, 80 (2008) 5986-5992.
[23] K.L. Moore, M. Schröder, C.R. Grovenor, Imaging secondary ion mass spectroscopy, Handbook of Nanoscopy, Volume 1&2, (2012) 709-744.
[24] M.A. Robinson, D.J. Graham, D.G. Castner, ToF-SIMS Depth Profiling of Cells: z-Correction, 3D Imaging, and Sputter Rate of Individual NIH/3T3 Fibroblasts, Anal Chem, 84 (2012) 4880-4885.
[25] B. Tomiyasu, I. Fukuju, H. Komatsubara, M. Owari, Y. Nihei, High spatial resolution 3D analysis of materials using gallium focused ion beam secondary ion mass spectrometry (FIB SIMS), Nucl Instrum Meth B, 136 (1998) 1028-1033.
[26] R.J. Chater, I. Corni, A.R. Boccaccini, M.P. Ryan, Three-dimensional reconstruction of a nickel-alumina composite coating by FIB-SIMS, Surf Interface Anal, 43 (2011) 492-494.
[27] Y. Fleming, T. Wirtz, High sensitivity and high resolution element 3D analysis by a combined SIMS-SPM instrument, Beilstein J Nanotech, 6 (2015) 1091-1099.
[28] T. Wirtz, Y. Fleming, U. Gysin, T. Glatzel, U. Wegmann, E. Meyer, U. Maier, J. Rychen, Combined SIMS-SPM instrument for high sensitivity and high-resolution elemental 3D analysis, Surf Interface Anal, 45 (2013) 513-516.
[29] C. Poczatek, Z. Kaufman, C. Lechene, OpenMIMS ImageJ Plugin Guide, Harvard Medical School (Boston, Massachusetts, USA), (2009) 1-18.
[30] ThermoFisher, https://www.fei.com/software/amira-avizo/, (2018).
[31] F.G. Rudenauer, Spatially Multidimensional Secondary-Ion Mass-Spectrometry Analysis, Anal Chim Acta, 297 (1994) 197-230.
[32] M.L. Wagter, A.H. Clarke, K.F. Taylor, P.A.W. vanderHeide, N.S. McIntyre, Topographic correction of 3D SIMS images, Surf Interface Anal, 25 (1997) 788-789.
[33] B. de Gabory, A.T. Motta, K. Wang, Transmission electron microscopy characterization of Zircaloy-4 and ZIRLO (TM) oxide layers, J Nucl Mater, 456 (2015) 272-280.
[34] C. Magee, R. Honig, Depth profiling by SIMS—depth resolution, dynamic range and sensitivity, Surf Interface Anal, 4 (1982) 35-41.
[35] N. Ni, S. Lozano-Perez, J.M. Sykes, G.D.W. Smith, C.R.M. Grovenor, Focussed ion beam sectioning for the 3D characterisation of cracking in oxide scales formed on commercial ZIRLO (TM) alloys during corrosion in high temperature pressurised water, Corros Sci, 53 (2011) 4073-4083.
[36] A.T. Motta, A. Couet, R.J. Comstock, Corrosion of Zirconium Alloys Used for Nuclear Fuel Cladding, Annu Rev Mater Res, 45 (2015) 311-343.
[37] M. Tupin, C. Bisor, P. Bossis, J. Chene, J.L. Bechade, F. Jomard, Mechanism of corrosion of zirconium hydride and impact of precipitated hydrides on the Zircaloy-4 corrosion behaviour, Corros Sci, 98 (2015) 478-493.
[38] H. Muta, Y. Etoh, Y. Ohishi, K. Kurosaki, S. Yamanaka, Ab initio study of hydrogen diffusion in zirconium oxide, J Nucl Sci Technol, 49 (2012) 544-550.
[39] D. Khatamian, F. Manchester, An ion beam study of hydrogen diffusion in oxides of Zr and Zr-Nb (2.5 wt%): I. Diffusion parameters for dense oxide, J Nucl Mater, 166 (1989) 300-306.
[40] I. Takagi, K. Une, S. Miyamura, T. Kobayashi, Deuterium diffusion in steam-corroded oxide layer of zirconium alloys, J Nucl Mater, 419 (2011) 339-346.

[41] N.S. Mcintyre, R.D. Davidson, C.G. Weisener, B.D. Warr, M.B. Elmoselhi, Sims Studies of Hydrogen Diffusion through Oxides on Zr-Nb Alloy, Surf Interface Anal, 17 (1991) 757-763.
[42] A. Coueta, A.T. Motta, R.J. Comstock, Hydrogen pickup measurements in zirconium alloys: Relation to oxidation kinetics, J Nucl Mater, 451 (2014) 1-13.
[43] J.F. Ziegler, M.D. Ziegler, J.P. Biersack, SRIM–The stopping and range of ions in matter (2010), Nuclear Instruments and Methods in Physics Research Section B: Beam Interactions with Materials and Atoms, 268 (2010) 1818-1823.
[44] T. Ishitani, H. Kaga, Calculation of local temperature rise in focused-ion-beam sample preparation, Journal of Electron Microscopy, 44 (1995) 331-336.
[45] R. Schmied, J.E. Fröch, A. Orthacker, J. Hobisch, G. Trimmel, H. Plank, A combined approach to predict spatial temperature evolution and its consequences during FIB processing of soft matter, Physical Chemistry Chemical Physics, 16 (2014) 6153-6158.
[46] S. Mahmood, D. Farkas, R. Adamson, Y. Etoh, Zirconium in the Nuclear Industry: 12th International Symposium, ASTM STP, 1354 (2000) 139-169.